JCI insight

RESEARCH ARTICLE

Multipanel mass cytometry reveals anti–PD-1 therapy–mediated B and T cell compartment remodeling in tumor-draining lymph nodes

Won Jin Ho,[1,2] Mark Yarchoan,[1,2] Soren Charmsaz,[1,2] Rebecca M. Munday,[3] Ludmila Danilova,[1,2,4] Marcelo B. Sztein,[5,6,7,8] Elana J. Fertig,[1,2,3,4,9,10] and Elizabeth M. Jaffee[1,2,7,11,12]

[1]Sidney Kimmel Comprehensive Cancer Center, [2]Bloomberg-Kimmel Institute for Cancer Immunotherapy, [3]McKusick-Nathans Institute for Genetic Medicine, and [4]Division of Biostatistics and Bioinformatics, Department of Oncology, Johns Hopkins University School of Medicine, Baltimore, Maryland, USA. [5]Center for Vaccine Development and Global Health, [6]Graduate Program in Molecular Microbiology and Immunology, Graduate Program in Life Sciences, [7]Department of Pediatrics, and [8]Department of Medicine, University of Maryland School of Medicine, Baltimore, Maryland, USA. [9]Department of Biomedical Engineering and [10]Department of Applied Mathematics and Statistics, Johns Hopkins University, Baltimore, Maryland, USA. [11]Pancreatic Cancer Precision Medicine Program and [12]Department of Pathology, Johns Hopkins University School of Medicine, Baltimore, Maryland, USA.

Anti–programmed cell death protein 1 (anti–PD-1) therapy has become an immunotherapeutic backbone for treating many cancer types. Although many studies have aimed to characterize the immune response to anti–PD-1 therapy in the tumor and in the peripheral blood, relatively less is known about the changes in the tumor-draining lymph nodes (TDLNs). TDLNs are primary sites of tumor antigen exposure that are critical to both regulation and cross-priming of the antitumor immune response. We used multipanel mass cytometry to obtain a high-parameter proteomic (39 total unique markers) immune profile of the TDLNs in a well-studied PD-1–responsive, immunocompetent mouse model. Based on combined hierarchal gating and unsupervised clustering analyses, we found that anti–PD-1 therapy enhances remodeling of both B and T cell compartments toward memory phenotypes. Functionally, expression of checkpoint markers was increased in conjunction with production of IFN-γ, TNF-α, or IL-2 in key cell types, including B and T cell subtypes, and rarer subsets, such as Tregs and NKT cells. A deeper profiling of the immunologic changes that occur in the TDLN milieu during effective anti–PD-1 therapy may lead to the discovery of novel biomarkers for monitoring response and provide key insights toward developing combination immunotherapeutic strategies.

Introduction

Tumor-draining lymph nodes (TDLNs) are one of the primary sites of tumor antigen exposure and antigen-specific immune activation, a barrier between local and systemic immune responses. TDLNs are, however, also major sites of immune regulation, contributing to the expansion and suppressive action of immunosuppressive populations, such as Tregs and myeloid-derived suppressor cells (MDSCs) (1–4). Previous studies have shown that the tumor antigen–experienced TDLNs exhibit a disproportionately increased B cell compartment relative to the T cell compartment (5–8). Furthermore, regulatory B cells (Bregs) accumulate locally in the TDLNs and promote tumor growth (9, 10). These factors present TDLNs as one of the primary targets of immune modulation for improving antitumor immunotherapeutic strategies through a better understanding of their role in tumor progression (11, 12).

Immunotherapy agents' targeting of the programmed cell death protein 1 (PD-1) pathway has led to unprecedented responses in multiple cancer types (13). By antagonizing PD-1, an inhibitory checkpoint molecule expressed on the surface of exhausted T cells, the immune system is reinvigorated to attack cancer cells (14). In contrast to the described immunoregulatory effects of TDLNs, a recent study has also demonstrated that TDLNs are a critical component of the antitumor immune response to anti–PD-1

Conflict of interest: MY reports receiving a commercial research grant from Bristol-Myers Squibb, Exelixis, and Merck & Co and is a consultant/advisory board member for Eisai and Exelixis. EJF is a consultant for Champions Oncology. EMJ reports receiving a commercial research grant from Bristol-Myers Squibb, Aduro Biotech, and Amgen; has ownership interest (including stock, patents, etc.) in Aduro Biotech; and is a consultant/advisory board member for CStone, Dragonfly, Genocea, and Adaptive Biotechnologies.

Submitted: August 5, 2019
Accepted: December 12, 2019
Published: January 30, 2020.

Reference information: *JCI Insight*. 2020;5(2):e132286. https://doi.org/10.1172/jci.insight.132286.

therapy (15). Although there have been significant efforts to characterize the changes in the immune tumor microenvironment and peripheral blood with anti–PD-1 therapy, the impact of anti–PD-1 therapy on the immunologic makeup of TDLNs remains largely unexplored.

To study TDLNs, we established an immunocompetent syngeneic mouse model by injecting MC38 colon carcinoma cells subcutaneously into the right hind limb of C57BL/6 mice, permitting direct interrogation of the TDLN at the right inguinal lymph node. The immunologic phenotype of this model is also well known for its responsiveness to anti–PD-1 therapy, and the changes occurring in the tumor-infiltrating immune cells have previously been characterized (16).

To study in depth both T and B cell subtypes and their functional status within TDLNs, we used multipanel mass cytometry, cytometry by time-of-flight (CyTOF) (17), and performed single-cell proteomic profiling of the TDLN using 39 unique markers. To enable a more robust downstream analysis, we also used a multiplexed staining approach based on CD45 barcoding. By both unsupervised clustering and hierarchal gating analysis of the debarcoded CyTOF data sets, we found that anti–PD-1 therapy preferentially modulated the B cell compartment, with skewing toward mature and memory phenotypes favored in both B and T cells. Analysis of functional marker expression in these B and T cell subsets demonstrated that CD69, checkpoint, and specific inflammatory cytokine expression are enhanced by anti–PD-1 therapy in memory B and T cells and that these changes occur in association with an increase in a subset of Tregs that produce TNF-α and NKT cells that produce IL-2.

Results

TDLNs are increased in size in response to anti–PD-1 therapy. To study the changes in TDLNs in response to anti–PD-1 therapy, we studied a well-established mouse model of PD-1 responsiveness, MC38 colon cancer cells, in a syngeneic C57BL/6 background. Mice were injected subcutaneously in the right hind limb with MC38 cells and were treated with isotype or anti–PD-1 antibody on days 14 and 18 when tumors reached approximately 500 mm^3 in volume; tumor volumes and TDLNs were assessed on day 21 (Figure 1A). As expected, tumor volumes were smaller in the anti–PD-1 group (Supplemental Figure 1A; supplemental material available online with this article; https://doi.org/10.1172/jci.insight.132286DS1). Based on weight (Figure 1B) and cellularity (Figure 1C), TDLNs were significantly larger than the right inguinal lymph nodes from non–tumor-bearing normal mice, and PD-1–treated TDLNs were significantly larger than isotype-treated TDLNs. There were no significant differences in the TDLN size whether the mice were untreated or treated with the isotype antibody (Supplemental Figure 1, B and C).

Increase in TDLN size related to anti–PD-1 therapy is due to disproportionate expansion of the B cell compartment. To analyze the immune cell constituents of TDLNs, 3 groups were cross-compared: anti–PD-1–treated TDLNs, isotype-treated control TDLNs, and naive lymph nodes from non–tumor-bearing normal mice as an additional control comparator. Lymph nodes were dissociated into single cells and subjected to PMA/ionomycin stimulation to simultaneously determine the immune cell capacity for cytokine production along with their subtyping markers. Samples belonging to each of the 3 groups were barcoded by staining with a CD45 antibody conjugated to a unique metal tag. CD45-labeled cells from each group were then combined into 3-plex batches. The batches were subsequently aliquoted for multiplexed staining with either T or B cell–oriented CyTOF panels as shown in Figure 1D and Supplemental Tables 1 (for T cells) and 2 (for B cells). Hierarchical gating on biaxial plots to identify T and B cell compartments identified the following subsets: naive and memory cytotoxic T cells, naive and memory helper T cells, Tregs, T1- and T2-type transitional B cells, mature phenotype B cells, memory B cells, and Bregs (gating strategies shown in Supplemental Figures 2 and 3). These analyses revealed that anti–PD-1 therapy significantly expanded both B and T cell populations but with more pronounced effects on B cells (Figure 2A). Compared with non–tumor-bearing naive lymph nodes, isotype-treated TDLNs exhibited 2.2-fold and 11.7-fold expansions in the T and B cell compartments, respectively, whereas anti–PD-1–treated TDLNs showed 4.7-fold T cell and 28.0-fold B cell compartment expansions. Further gating was done to profile subsets of both B and T cell compartments within the TDLNs (Figure 2B and Supplemental Figure 4). No significant differences in the TDLNs were attributable to the isotype antibody itself (Supplemental Figure 1D). In parallel, we also performed unsupervised clustering analysis using the FlowSOM algorithm. Using the T cell–oriented and B cell–oriented CyTOF panels, we identified 20 and 25 metaclusters that were then annotated into 7 T cell subtypes (Figure 3A) and 10 B cell subtypes (Figure 4A), respectively. All cell type annotations are listed in Supplemental Table 3. In terms of cell numbers of each cell type in each lymph node, most cell types

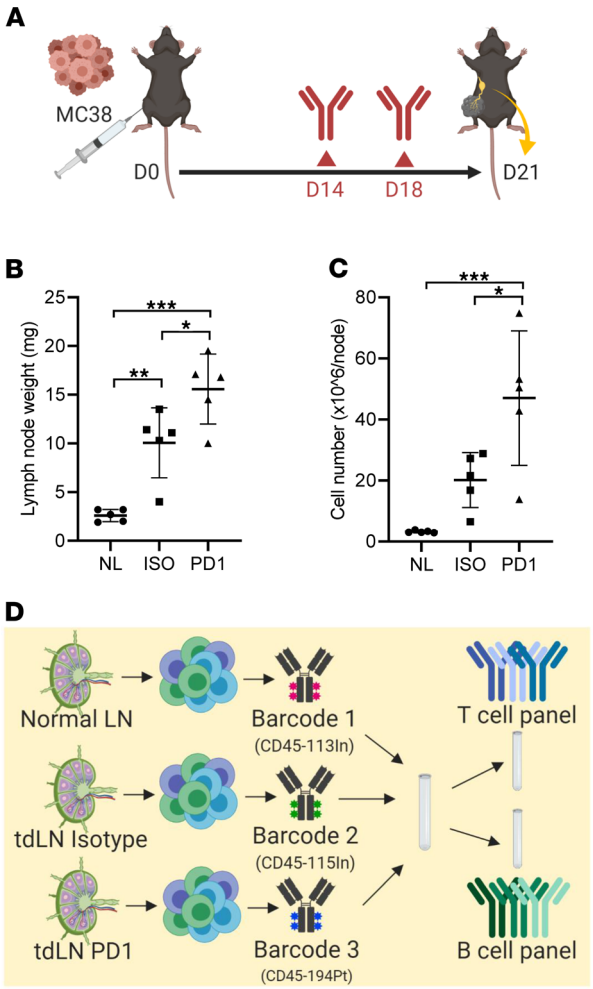

Figure 1. Experimental schema for analyzing TDLNs during effective anti–PD-1 therapy. (**A**) MC38 tumor cells were injected subcutaneously at day 0 (D0) in the right hind limb of C57BL/6 mice, and either isotype (ISO) or PD-1 antibody (PD-1) was administered intraperitoneally on D14 and D18. Right inguinal lymph nodes were harvested on D21 for analysis. Lymph nodes at the same location from normal, non–tumor-bearing mice (NL) were used as additional control comparators. (**B**) Lymph nodes were weighed on D21 upon harvest, and (**C**) absolute number of cells was counted from each lymph node. Mean ± SD (n = 5) are shown for both plots. (**D**) Schematic shows how lymph nodes from each respective group (Normal LN, non–tumor-bearing normal mice; tdLN Isotype, isotype-treated tumor-bearing mice; tdLN PD-1, PD-1–antibody–treated tumor-bearing mice) were barcoded with a specific CD45 antibody tagged with a unique metal to be multiplexed and stained with a T or B cell subtyping mass cytometry panel. Results for repeated-measures ANOVA followed by pairwise testing are shown as FDR-adjusted $^{*}P \le 0.05$; $^{**}P \le 0.01$; and $^{***}P \le 0.005$.

were significantly increased by anti–PD-1 therapy compared with isotype controls (Figure 3B and Figure 4B). This was especially true for memory B and T cells and regulatory B and T cells (Figure 3C, Figure 4C, and Supplemental Figure 5). Thus, our data suggest that anti–PD-1 therapy stimulates T cell expansion and even greater B cell expansion, along with differentiation leading to significant increases in the presence of both memory and regulatory subtypes.

Anti–PD-1 therapy augments differentiation of B and T cell types away from naive and toward memory and mature subtypes, especially for B cells. To further evaluate how each of the B and T cell compartments are remodeled by anti–PD-1 therapy, we used the same CyTOF data sets to then analyze the subtypes as percentages within each of the T or B cell compartments. As visualized by a dimensionality reduction algorithm, uniform manifold approximation and projection (UMAP) (Figure 5A and Figure 6A), the anti–PD-1 therapy group demonstrated the highest percentage of memory T cells, both CD4 and CD8, and the lowest percentage of naive T cells in the T cell compartment (Figure 5B). Similarly, the highest percentage of memory B cell types and the lowest percentage of immature/transitional B cell types were generally noted in the anti–PD-1 therapy group (Figure 6B). Among all the B and T cell types analyzed (Supplemental Figures 6 and 7), statistically significant differences between isotype and anti–PD-1 therapy were particularly noted for memory "B1" ($CD21^{+}CD23^{+}CD38^{+}B220^{hi}IgD^{hi}IgM^{hi}$, 1.55-fold vs. 1.37-fold change relative to non–tumor-bearing lymph node) and memory "B3" ($CD21^{+}CD23^{+}CD38^{+}B220^{hi}IgD^{hi}IgM^{lo}$, 1.41-fold vs. 0.9-fold change relative to non–tumor-bearing lymph node) subtypes.

Next, we performed a repeat run of the experiment with a different CyTOF panel to further validate these observations. This CyTOF panel was modified to (a) combine T and B subtyping markers into a single simplified panel, (b) replace $CD3^{+}CD4^{+}CD25^{+}CD127^{-}$ with $CD3^{+}CD4^{+}Foxp3$ as the canonical combination of markers to identify Tregs, and (c) exclude cytokine assaying to profile the lymph nodes

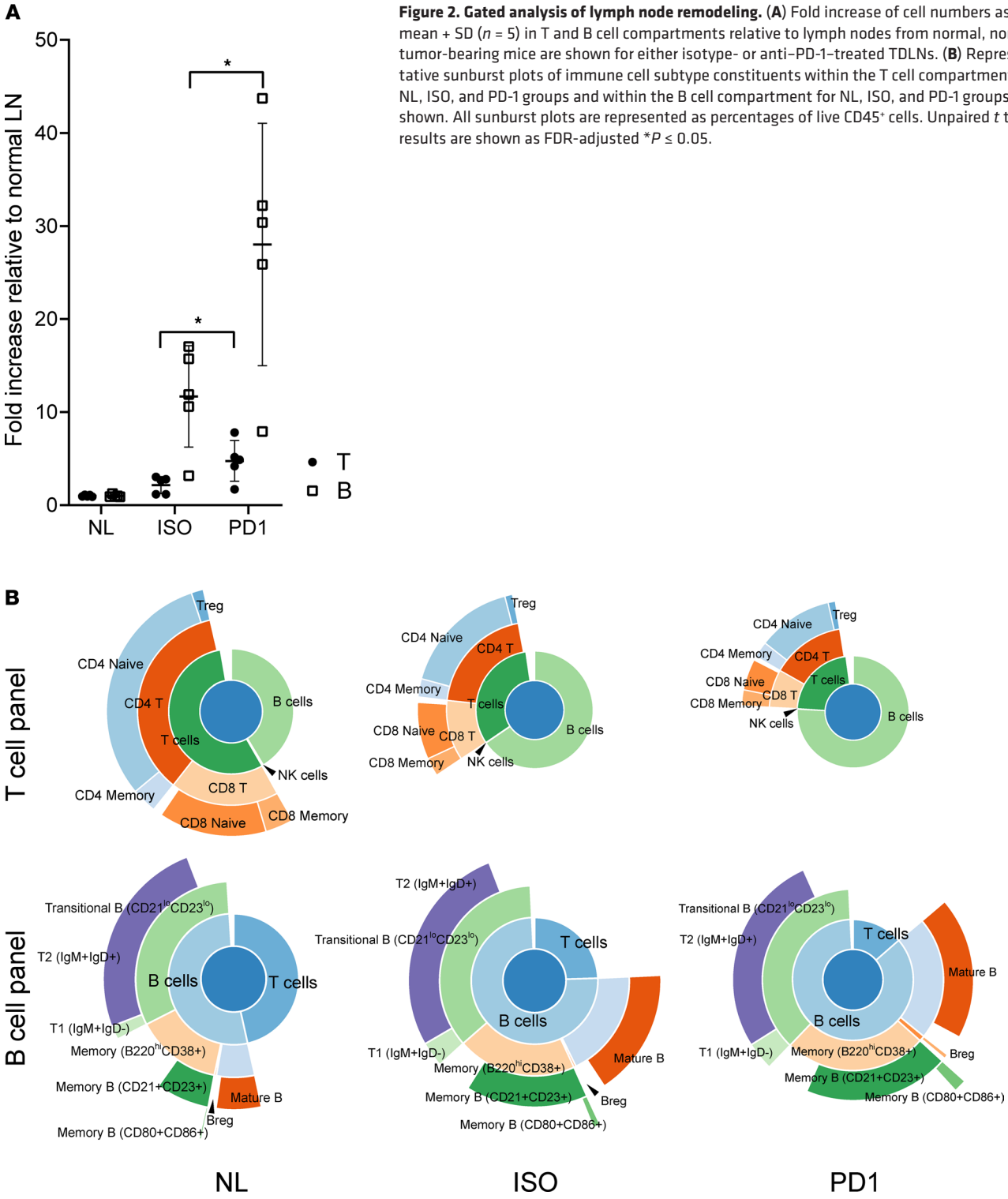

Figure 2. Gated analysis of lymph node remodeling. (**A**) Fold increase of cell numbers as mean + SD (n = 5) in T and B cell compartments relative to lymph nodes from normal, non–tumor-bearing mice are shown for either isotype- or anti–PD-1–treated TDLNs. (**B**) Representative sunburst plots of immune cell subtype constituents within the T cell compartment for NL, ISO, and PD-1 groups and within the B cell compartment for NL, ISO, and PD-1 groups are shown. All sunburst plots are represented as percentages of live CD45$^+$ cells. Unpaired t test results are shown as FDR-adjusted $^*P \leq 0.05$.

without a stimulation step (Supplemental Table 4). Based on the metal intensities from 18 subtyping markers, we performed FlowSOM and UMAP algorithms again for this data set to identify and annotate the 25 metaclusters into 7 T cell clusters, 4 B cell clusters, and 1 NK cell cluster (Supplemental Figure 8 and Supplemental Table 5). We also performed, in parallel, hierarchal gating of the cell subtypes as performed previously. Based on the results from both analytical approaches, the anti–PD-1 effects on the T cell compartment were consistent, again showing significant increases in memory and regulatory phenotypes (Supplemental Figures 9–12). Moreover, the dramatic increases in B cells within the TDLNs were

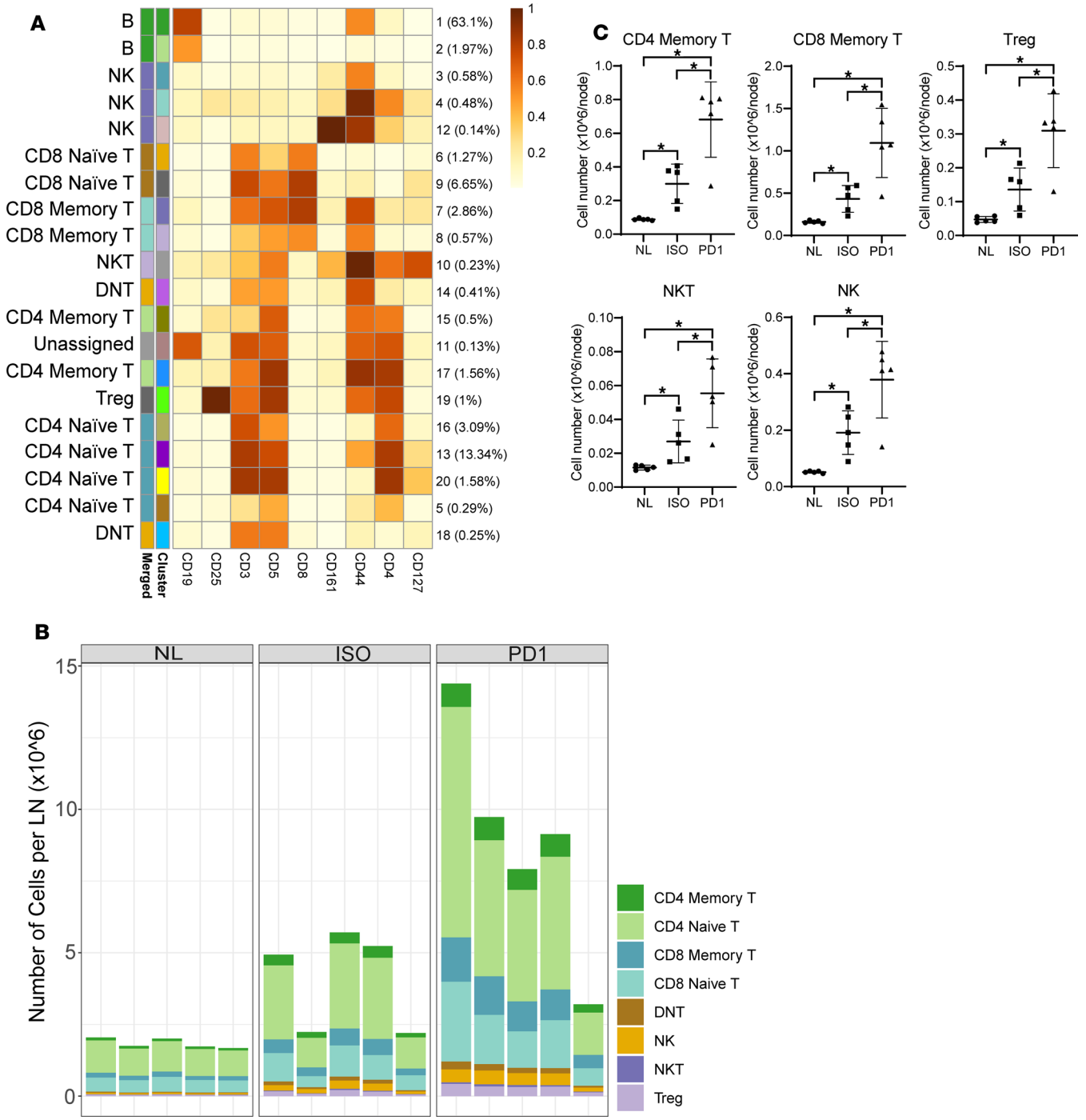

Figure 3. Unsupervised analysis of lymph node remodeling in the T cell compartment. (**A**) Based on the data set from 9 canonical markers in the T cell subtyping mass cytometry panel, FlowSOM algorithm was used to yield 20 metaclusters annotated into 10 final clusters. The resulting phenograph for all the samples in the data set is shown. (**B**) Number of cells per lymph node within each of the T cell clusters is shown for each individual mouse for all 3 groups. (**C**) Numbers of cells per lymph node for 5 key T cell clusters are summarized in scatter plots with mean ± SD (n = 5) for the 3 groups, non–tumor-bearing mice, isotype-treated mice, and anti–PD-1–treated mice. Results for repeated-measures ANOVA followed by pairwise testing are shown as FDR-adjusted *$P \leq 0.05$. Breg, regulatory B cells; Imm, immature; Mat, mature.

confirmed by this repeat data set; i.e., the B cell compartment was the predominant component enhanced within the TDLNs. Although the effects of anti–PD-1 therapy on the B cell compartment remodeling within the TDLNs were less robust in this repeat set, mild trends could be observed for the memory subtype cells and Bregs. The tumor itself appears to affect the B cell compartment within TDLNs, and this may be enhanced with anti–PD-1 therapy.

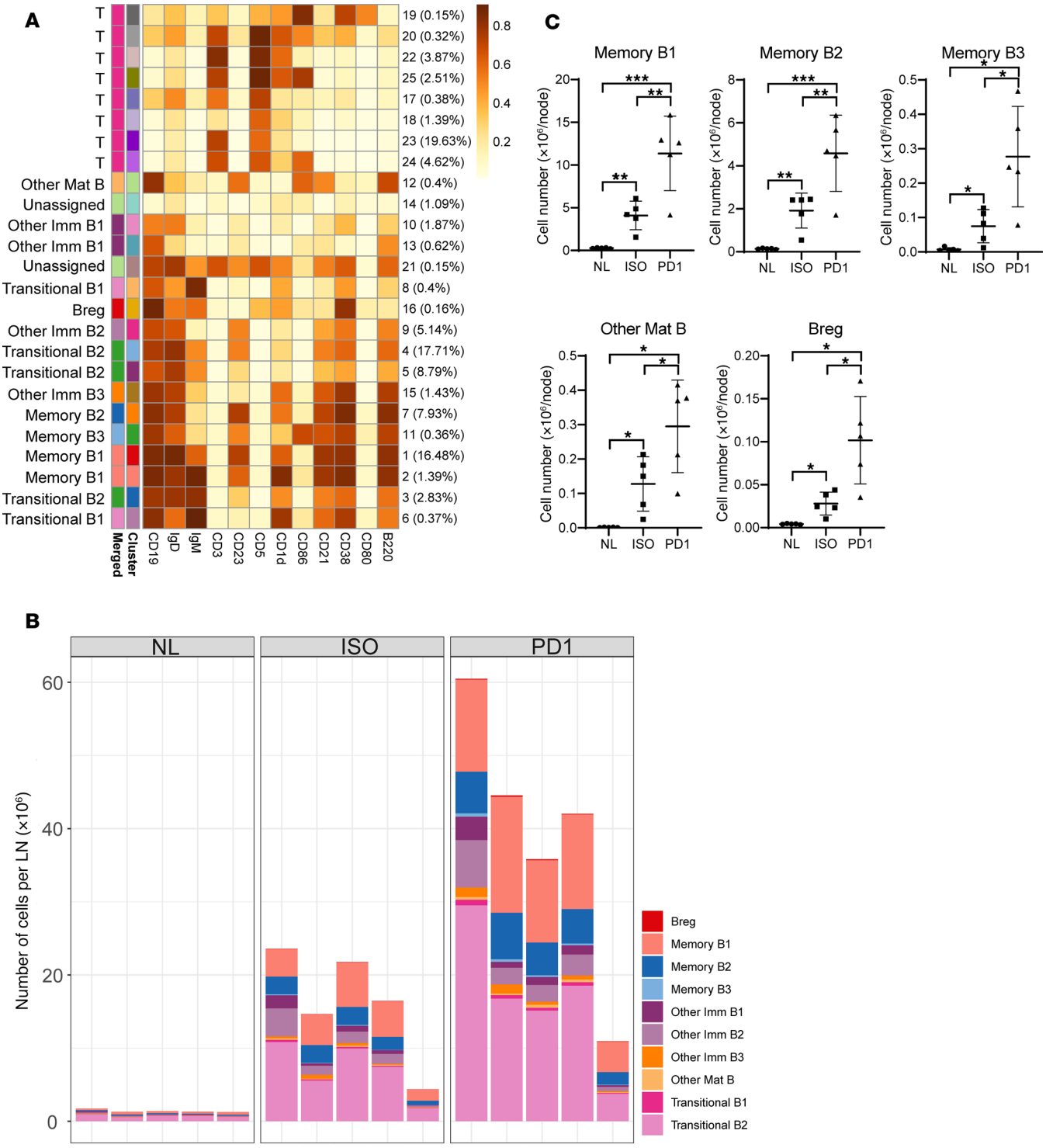

Figure 4. Unsupervised analysis of lymph node remodeling in the B cell compartment. (**A**) Based on the data set from 12 canonical markers in the B cell subtyping mass cytometry panel, FlowSOM algorithm was used to yield 25 metaclusters annotated into 12 final clusters. The resulting phenograph for all the samples in the data set is shown. (**B**) Number of cells per lymph node within each of the B cell clusters is shown for each individual mouse for all 3 groups. (**C**) Numbers of cells per lymph node for 5 key B cell clusters are summarized in scatter plots with mean ± SD bars for the 3 groups, non–tumor-bearing mice, isotype-treated mice, and anti–PD-1–treated mice. Results for repeated-measures ANOVA followed by pairwise testing are shown as FDR-adjusted $*P \le 0.05$; $**P \le 0.01$; and $***P \le 0.005$. DNT, double-negative T cells; NK, natural killer cells; NKT, natural killer T cells; Treg, regulatory T cells.

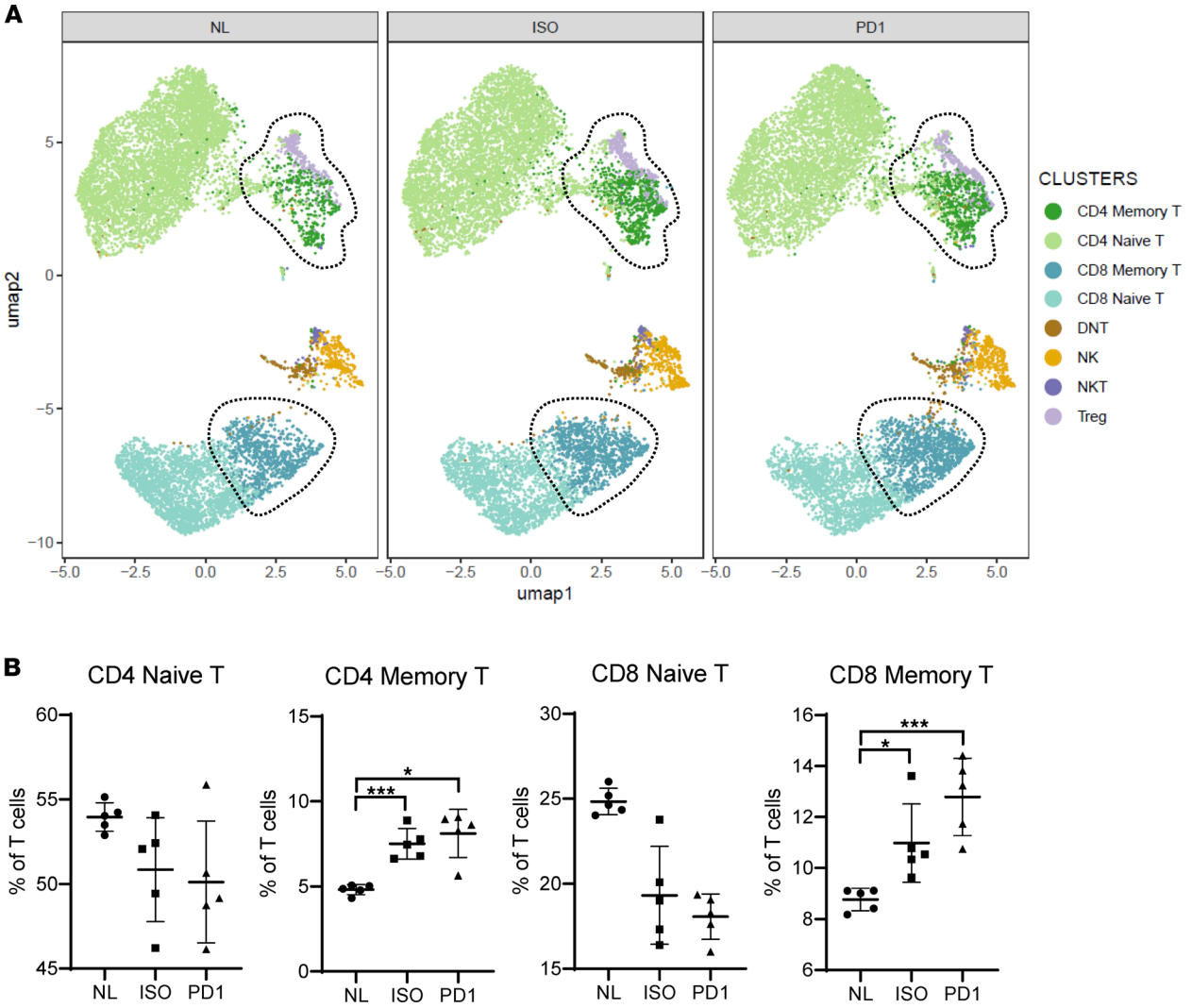

Figure 5. Profiling the T cell compartment remodeling as proportions within each lymph node. Representative UMAP plots for dimensionality reduction and visualization of the T cell clusters (**A**) for the 3 groups, non–tumor-bearing mice, isotype-treated mice, and anti–PD-1–treated mice. Dotted lines encircle memory phenotype clusters. Relative proportions of 4 key T cell clusters (**B**) within each lymph node are summarized as scatter plots with mean ± SD (n = 5) for the 3 groups. Results for repeated-measures ANOVA followed by pairwise testing are shown as FDR-adjusted $^*P \le 0.05$; $^{***}P \le 0.005$.

Lymph node remodeling is specific to successful response to anti–PD-1 therapy in tumor-bearing mice but not in normal mice without tumors. Because the observed changes in the B and T cell compartments could just represent nonspecific changes occurring with PD-1 inhibition, we also assessed by both CyTOF and flow cytometry the impact of anti–PD-1 therapy in the lymph nodes from normal, non–tumor-bearing mice and contralateral (non–tumor-draining) lymph nodes from MC38-bearing mice. Except for nonsignificant minimal trends, treatment with anti–PD-1 therapy did not have any notable impact in the lymph nodes from normal mice (Supplemental Figure 13). However, in the contralateral site in MC38-bearing mice, there were increased numbers of B and T cell subtypes in the tumor-bearing non–tumor-draining lymph nodes (Supplemental Figures 9–12). Furthermore, when we assessed the TDLNs from mice bearing B16-F10 tumors, which are classically known to be PD-1 resistant (Supplemental Figure 14A), no significant differences were detected between the isotype and anti–PD-1 therapy groups within the TDLNs across all B and T cell types analyzed (Supplemental Figure 14B). These findings together suggest that the TDLN is an active site of response to PD-1 therapy and that the drastic remodeling within the lymph nodes is unique to successful PD-1 therapy in tumor-exposed immune responses.

Functional activation by anti–PD-1 therapy occurs in both B and T cell compartments. Expression of functional markers was analyzed by 2 parallel approaches: (a) proportional gating of cells with relatively

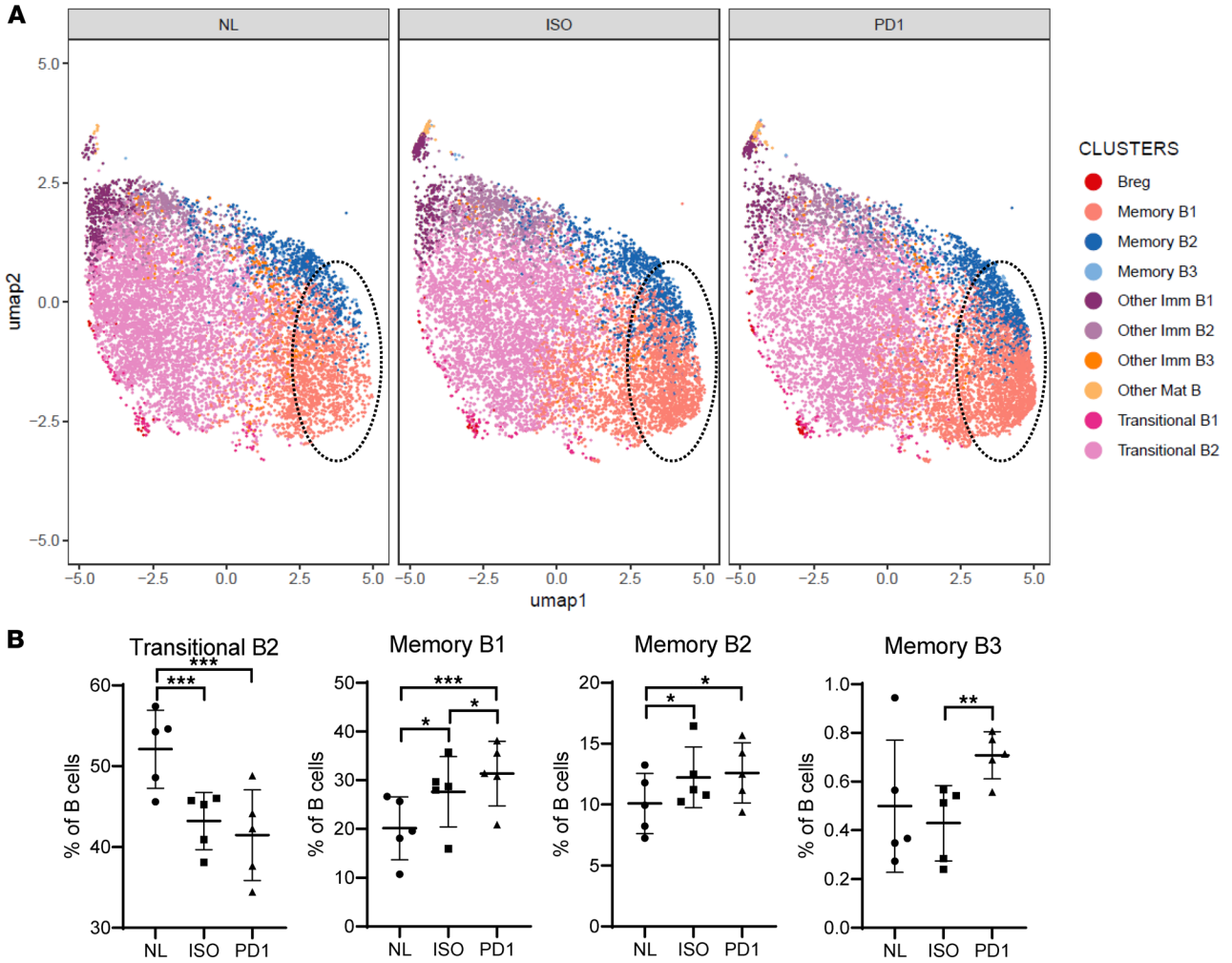

Figure 6. Profiling the B cell compartment remodeling as proportions within each lymph node. Representative UMAP plots for dimensionality reduction and visualization of the B cell clusters (**A**) for the 3 groups, non–tumor-bearing mice, isotype-treated mice, and anti–PD-1–treated mice. Dotted lines encircle memory phenotype clusters. Relative proportions of 4 key B cell clusters (**B**) within each lymph node are summarized as scatter plots with mean ± SD (n = 5, representing 1 multiplexed CyTOF run) for the 3 groups. Results for repeated-measures ANOVA followed by pairwise testing are shown as FDR-adjusted *$P \leq 0.05$; **$P \leq 0.01$; and ***$P \leq 0.005$.

high expression of each marker within each of the B and T cell subpopulations and (b) comparing median expression of the markers within the FlowSOM-clustered populations. As expected, expression of checkpoint markers was upregulated in TDLNs with anti–PD-1 therapy. In the T cell compartment, PD-1 expression was significantly higher in anti–PD-1–treated TDLNs compared with isotype-treated TDLNs for most cell types by gating analysis (Supplemental Figure 15, A–E) and for memory CD4$^+$ T cells and Tregs by median expression analysis of clusters (Figure 7, B–D, and Supplemental Figure 16). Similarly, by both analytical approaches, CTLA4 and Lag3 were expressed at the highest levels in the anti–PD-1 therapy group, especially in memory CD4$^+$ T cells and Tregs (Figure 7, E–G; Supplemental Figure 15, F–O; and Supplemental Figure 17). Programmed cell death protein ligand 1 (PD-L1) expression was also upregulated significantly by anti–PD-1 therapy in all T cell types (Supplemental Figure 18). In the B cell compartment, PD-L1 was upregulated significantly by anti–PD-1 therapy in transitional, memory, and Breg cell types (Figure 8, A, B, and D; Supplemental Figure 19, A–F; and Supplemental Figure 20). The expression of the costimulatory marker, CD40, was the highest in the anti–PD-1 therapy group for multiple B cell types (Supplemental Figure 19, G–L, and Supplemental Figure 21), especially transitional "B2" (CD19$^+$B220^{int}CD3$^-$CD21^{int}CD23^{int}IgM^{int}IgD^{hi}CD38^{int}CD86$^-$) and memory "B3" cell types (Figure 8, A, C, and E). Only slight differences, if any, were observed for the expression of B and T lymphocyte attenuator (BTLA), an inhibitory receptor (Supplemental Figure 19, M–R, and Supplemental Figure 22).

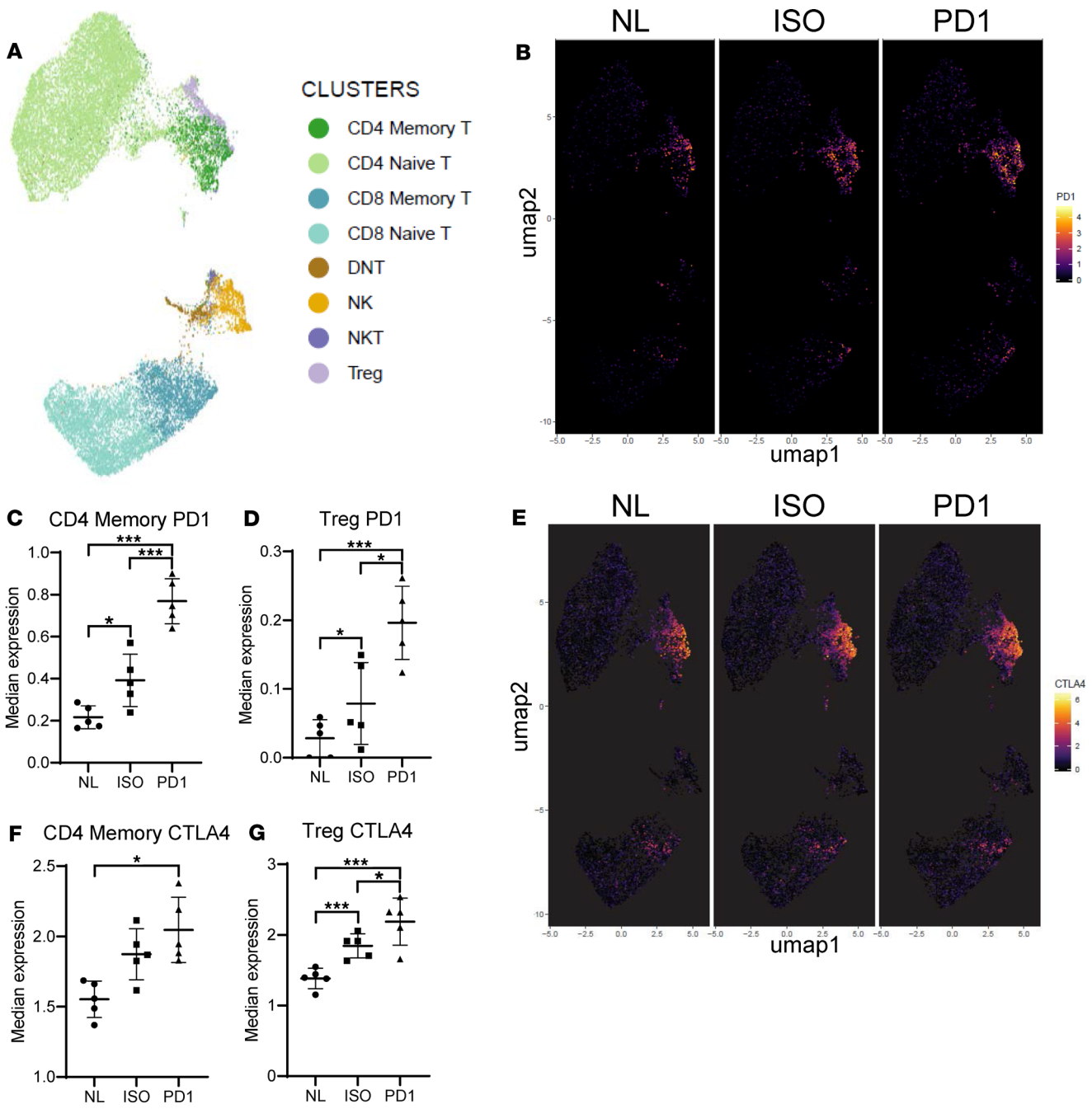

Figure 7. Checkpoint marker analysis of the T cell compartment. (**A**) All the T cell clusters identified by FlowSOM clustering are shown on the UMAP plot as a reference for other UMAP plots in the figure. Expression of PD-1 (**B**) and CTLA4 (**E**) is visualized in aggregate data from all samples as heatmaps superimposed on the T cell cluster UMAP plot shown in **A**. Median expressions of PD-1 (**C** and **D**) or CTLA4 (**F** and **G**) in CD4$^+$ memory (**C** and **F**) and Treg (**D** and **G**) subtypes are shown as scatter plots. Mean ± SD (n = 5) for non–tumor-bearing mouse lymph nodes, isotype-treated TDLNs, and anti–PD-1–treated TDLNs are represented as bars. Results for repeated-measures ANOVA followed by pairwise testing are shown as FDR-adjusted *$P \leq 0.05$; ***$P \leq 0.005$.

In addition to the checkpoint and costimulatory markers, production of 3 key inflammatory cytokines, IFN-γ, TNF-α, and IL-2, was also evaluated. IFN-γ levels were the highest in memory CD8$^+$ T cells among the T cell subtypes studied and were significantly increased with anti–PD-1 therapy (Figure 9, A and B; Supplemental Figure 23, A–E; and Supplemental Figure 24). TNF-α was also upregulated by PD-1 inhibition in memory T cells, primarily CD4$^+$ T cells (Figure 9, C and D; Supplemental Figure 23, F–J; and Supplemental Figure 25). Interestingly, our CyTOF analysis revealed a TNF-α–producing Treg population that anti–PD-1 therapy further enhanced. IL-2 expression was most prominent in memory CD4$^+$ T cells and was increased in response to anti–PD-1 therapy (Supplemental Figure 23, K–O, and Supplemental Figure 26).

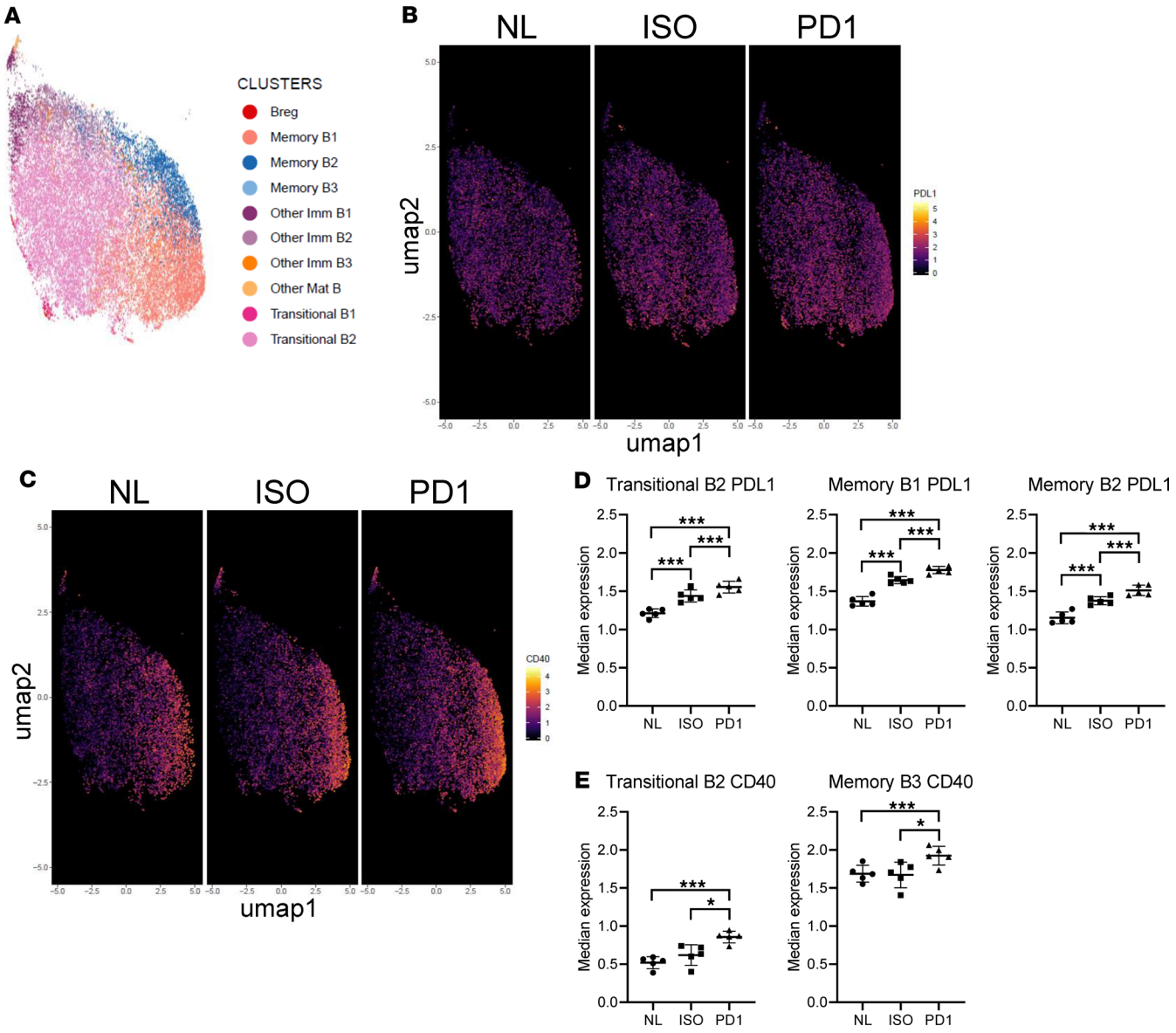

Figure 8. Functional analysis of the B cell compartment. (**A**) All the B cell clusters are shown on the UMAP plot as a reference for other UMAP plots in the figure. Expression of PD-L1 (**B**) and CD40 (**C**) is visualized in aggregate data from all samples as heatmaps superimposed on the B cell cluster UMAP plot shown in **A** with quantitative scatter plots showing mean ± SD (n = 5) of non–tumor-bearing mouse lymph nodes, isotype-treated TDLNs, and anti–PD-1–treated TDLNs for (**D**) PD-L1 in transitional B2, memory B1, and memory B2 subtypes and for (**E**) CD40 in transitional B2 and memory B3 subtypes. Results for repeated-measures ANOVA followed by pairwise testing are shown as FDR-adjusted *$P \leq 0.05$; ***$P \leq 0.005$.

Notably, IL-2 production in the rare NKT cell subset as well as in memory B cells (Supplemental Figures 27 and 28) was augmented significantly by anti–PD-1 therapy. In accordance with activation of B cells, CD69 expression was also moderately increased in multiple B cell subtypes in the PD-1–treated group (Supplemental Figure 29).

Discussion

Anti–PD-1 therapy has transformed the management of many human cancers, but only a subset of patients respond to anti–PD-1 therapy, and responses are rarely curative. Understanding the effects of anti–PD-1 therapy on the composition and functional state of tumor-associated immune subsets can identify mechanisms of response and resistance to anti–PD-1 therapy and provide insights into rational combination strategies to improve upon response rates to monotherapy. Although the effects of anti–PD-1 therapy within the tumor immune microenvironment in preclinical and human subjects have been

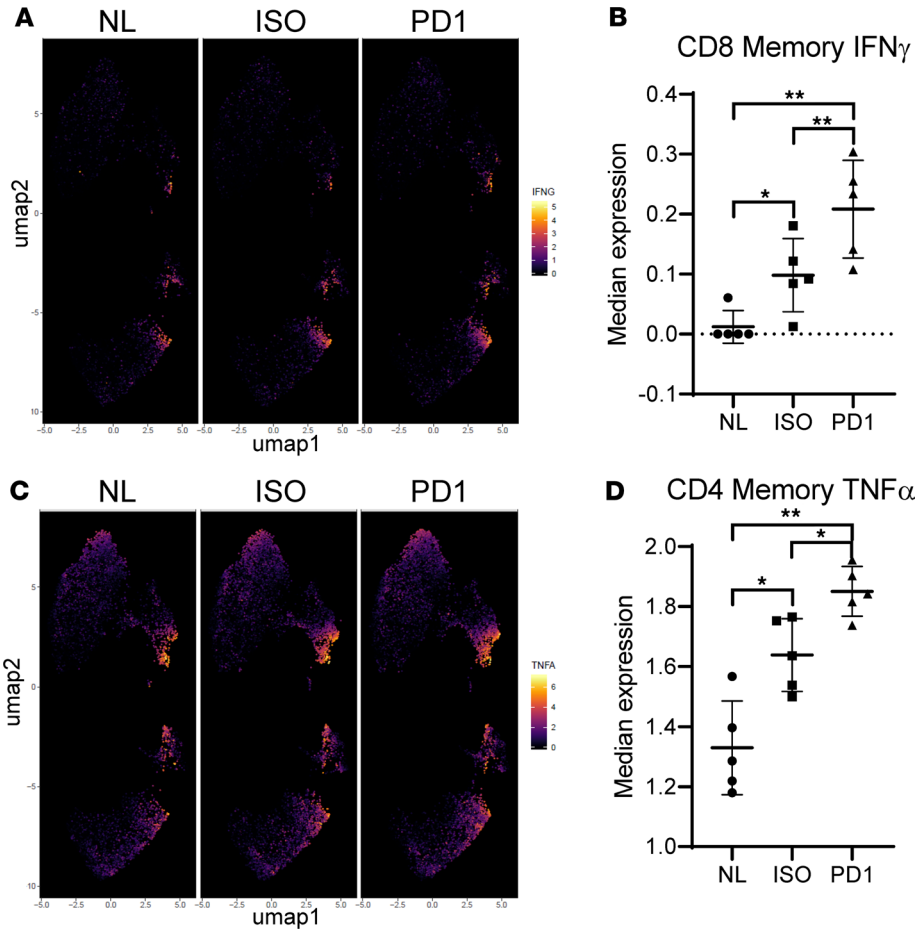

Figure 9. Cytokine analysis of the T cell compartment. Production of cytokines IFN-γ (**A**) and TNF-α (**C**) across all T cell clusters is visualized on the UMAP plots with corresponding scatter plots (**B** and **D**). Expression of the cytokines is visualized in aggregate data from all samples as heatmaps superimposed on the T cell cluster UMAP plot shown in Figure 7A. Results for repeated-measures ANOVA followed by pairwise testing are shown as FDR-adjusted $*P \leq 0.05$; $**P \leq 0.01$.

previously reported (13), to our knowledge this is the first study to broadly characterize the effects of anti–PD-1 therapy on TDLNs. Studying the TDLN is particularly valuable because it is one of the primary sites at which the tumor antigen exposure occurs and affects the immune response. Furthermore, to interrogate the changes in the B cell compartment, the TDLN offers an opportune site because within the tumors of many syngeneic immunocompetent mouse models, B cell presence is very rare (18), whereas in the peripheral blood, the findings would be even more removed from fully capturing direct responses to tumors. Our results regarding the immune cell type composition, checkpoint expression, and cytokine expression within TDLNs suggest that there are major remodeling events within the TDLN mediated by anti–PD-1 therapy that are critical for conferring effective antitumor immune responses. We demonstrate that B and T cell compartments and other cell subsets present at lower frequencies, such as NKT cells, undergo significant activation, expansion, and maturation in response to anti–PD-1 therapy, to shape antitumor programming in TDLNs. Importantly, our study provides a methodological demonstration that simultaneous use of complementary mass cytometry antibody panels enables deep interrogation of the immune profile and that performing unsupervised clustering and gating analyses in parallel empowers a more reliable and informative investigation.

Our results have important implications regarding the tumor immune response to anti–PD-1 therapy. First, assaying immune cell activation states in TDLNs may determine therapeutic responses and guide therapy development, including rational immunotherapy combinations. For example, we specifically identify a marked expansion of Bregs (PD-L1$^+$ B cells and CD5$^+$ B cells) in the TDLN in response to anti–PD-1 therapy. Bregs have been implicated in tumor progression because they may facilitate an

immunosuppressive environment and attenuate antitumor immune responses (19). This finding provides initial evidence that Bregs may be important for reestablishing tolerance in the setting of anti–PD-1 therapy, suggesting that therapies that inhibit Bregs may improve upon response to anti–PD-1 therapy. Second, our results show that anti–PD-1 therapy broadly reprograms the B cell component in TDLNs, highlighting the importance of exploring treatment strategies that target B cells to further enhance responses to PD-1–targeted therapies. This idea is consistent with the results of a previous study looking at non–small cell lung carcinoma demonstrating that B cell–mediated antigen presentation to $CD4^+$ T cells is a critical feature of effective antitumor immune response (20). We recognize, however, that targeting B cells successfully is not a simple goal given how B cells are involved in both protumor and antitumor programs, as extensively reviewed elsewhere (21). Third, our results provide new evidence of cytokine production changes within the TDLN milieu in response to PD-1 therapy that likely represent augmented antigen processing and presentation to activate both B and T cell subsets. For example, we find a significant increase in IL-2–producing memory B cells within the TDLN. Given the high number of B cells within the TDLN, our results indicate that B cells may be an important source of IL-2 that supports the antitumor T cell response. These IL-2–producing B cells also express higher levels of CD69, consistent with increased activation.

Interestingly, our high-parameter analysis also revealed a Treg subset producing increased TNF-α and NKT cells producing increased IL-2 in response to anti–PD-1 therapy. The role of TNF-α as an antitumor molecule and a stimulator of adaptive immunity is well established (22–25). Recent studies, however, have demonstrated that Tregs are maintained by TNF-α via TNF receptor 2 (26) and themselves produce TNF-α in response to activation, providing an autocrine immune–suppressive effect (27). Prior studies have also shown that TNF augments MDSC accumulation (28). In line with these reports, emerging evidence suggests blocking TNF-α may enhance anti–PD-1 therapy (29, 30). Thus, increased TNF-α in response to PD-1 inhibition observed in our data may represent both antitumor signaling and an immune-regulatory negative feedback loop. Prior studies have shown that NKT cells are able to stimulate the antigen-presenting functions of B cells (31) and secrete IL-2 upon activation to aid with reinvigoration of exhausted $CD8^+$ T cells (32). Thus, our data suggest that anti–PD-1 therapy is associated with activation of NKT cells that in turn further stimulate the antitumor immunological processes mediated by both B and T cells. Furthermore, these results provide new evidence that IL-2 and TNF-α accomplish this in TDLNs during anti–PD-1 therapy (33).

The study has the following conceptual limitations. First, we have not investigated further into the T cell receptor and B cell receptor immune repertoires or used a tumor antigen–specific model, e.g., ovalbumin-expressing MC38, which would elucidate the antigen specificity of the TDLN response. Second, the study evaluates a single time point only, limiting our understanding of how the TDLN remodeling occurs over time and whether a particular time point would be critical to assess. Third, because our study focuses on TDLNs, in which the vast majority of cells are lymphoid cells, it does not yield any insight into the interplay between lymphoid and myeloid immune compartments, which is also very important in shaping the antitumor immune response. Thus, it would be worthwhile to simultaneously assess the changes that occur within the tumor-infiltrating immune cells to understand the changes in the myeloid populations and delineate the unique features of the TDLN. Fourth, we have not demonstrated any causality of these findings with regard to the efficacy of anti–PD-1 therapy. This study thus prompts further investigations into the definitive roles of specific immune cell subtypes within the lymph nodes in the therapeutic outcome. Fifth, we demonstrate results from just 1 PD-1–responsive (MC38) and 1 PD-1–resistant (B16) model, restricting the generalized applicability of our conclusions. In light of these limitations, our findings are exploratory, warranting the need for more confirmatory and in-depth studies on changes that occur within the lymph nodes during anti–PD-1 therapy by incorporating additional animal models and treatment regimens.

In summary, we broadly characterized the composition and functional state of immune cell subsets within TDLNs in response to anti–PD-1 therapy in a PD-1 therapy–responsive tumor model. These data identified multiple immunological changes that may contribute to the activity of such agents, as well as potential mechanisms that may reestablish tolerance during anti–PD-1 therapy. A causal interrogation of each of the observed changes is needed to uncover the mechanisms underlying the observed phenomena. Moreover, our findings would be strengthened by extending these investigations to studies using clinical specimens. Our results suggest that the retrieval and analysis of TDLNs may enhance the evaluation of immunotherapy responses to this class of agents and should be integrated into neoadjuvant immunotherapy clinical trial designs.

Methods

Antibodies. A list of mass cytometry antibodies, isotopes, and concentrations used for a T cell subtyping panel and a B cell subtyping panel is in Supplemental Tables 1 and 2. Conjugation of primary antibodies (34) was performed using Maxpar Conjugation Kits according to the manufacturer's protocol (Fluidigm). Briefly, purified antibodies were run through a buffer exchange protocol using 50-kDa ultra filtration columns (Amicon) and then partially reduced with 4 mM Tris(2-carboxyethyl) phosphine hydrochloride (Thermo Fisher Scientific). Polymers were loaded individually with isotopically enriched metals 113In (Trace Sciences), 115In (MilliporeSigma), 163Dy (Fluidigm), and 175Lu (Fluidigm). Metal-loaded polymers were then conjugated to their respective antibodies and washed (see Supplemental Tables 1 and 2). 194Pt (Fluidigm) was directly conjugated to the reduced antibody. Antibody concentrations in the wash buffer were quantified using NanoDrop (Thermo Fisher Scientific). The final antibody concentrates were then diluted in a stabilization buffer (Candor) containing 0.3% sodium azide. Each antibody was titrated by testing a range of 3 to 4 serial dilutions of clear positive controls (e.g., stimulated lymphocytes for cytokine staining) and identifying the concentration that permits discrimination while minimizing spillover signals.

Animal model. Female 7-week-old C57BL/6J mice were purchased from The Jackson Laboratory and housed in the Johns Hopkins University animal facilities. Mice were allowed to acclimate for at least 1 week before experimentation. MC38 (Kerafast) cells were maintained in DMEM-based medium containing 10% FBS, 1% L-glutamine, 100 U/mL penicillin/streptomycin, 10 mM HEPES, 1 mM sodium pyruvate, and 0.1 mM nonessential amino acids (Life Technologies) in 5% CO_2 at 37°C. B16-F10 cells (ATCC) were maintained in RPMI 1640 with glutamine containing 10% FBS, 100 U/mL penicillin/streptomycin, 1 mM sodium pyruvate, and 0.1 mM nonessential amino acids. On day 0, 2.5×10^5 MC38 or 5×10^5 B16-F10 cells were injected subcutaneously into the right hind limb (16). Tumors were allowed to be established and grow for 2 weeks. Mice were then administered isotype or PD-1 antibody (clone RMP1-14, BioXCell) 10 mg/kg intraperitoneally on days 14 and 18. Tumor-draining right inguinal lymph nodes were identified and harvested for analysis on day 21. For assessment of non–tumor-draining lymph nodes, left inguinal lymph nodes were harvested. Tumor volume was also calculated on day 21 based on caliper-measured major (D) and minor (d) diameters using the following formula: $V = 1/2 \times D \times d^2$. Right inguinal lymph nodes from age-matched non–tumor-bearing normal mice were used as an additional control. Harvested lymph nodes were weighed and then processed into single-cell suspensions by manual dissociation through a 70-μM filter in PBS with 4 mM EDTA. Total cell numbers from individual lymph nodes were counted using a hemocytometer and recorded. For staining, 2×10^6 cells were plated into each well of a 96-well microplate.

Mass cytometry staining and data acquisition. Cells were stimulated in RPMI with 10% FBS containing 1× PMA/ionomycin/brefeldin A cocktail (BioLegend) for 3 hours in 5% CO_2 at 37°C. During the final 15 minutes, cells were incubated in medium containing 5 mM EDTA (35). After stimulation, cells were washed with PBS with 4 mM EDTA. Viability was marked by incubation in palladium chloride (MilliporeSigma) dissolved in DMSO and diluted in PBS to 500 nM for 5 minutes at room temperature, after which complete medium was used to quench the remaining palladium (36). TDLN cells from 1 mouse from each of the 3 groups were stained with a unique metal barcode tagged to CD45 for 25 minutes at room temperature (Figure 1D). Cells from these 3 animals were then combined into a single tube for downstream processing. Each tube was then divided into 2 equal aliquots and blocked with 1 μg anti-mouse Fc block (BD Biosciences) for 10 minutes at room temperature followed by a cocktail of antibodies for the T cell or the B cell panel (Figure 1D and Supplemental Tables 1 and 2). Surface marker staining was performed in cell staining buffers (Fluidigm) at room temperature for 30 minutes. Intracellular cytokine staining was performed using Cytofix/Cytoperm Kit (BD Biosciences) per the manufacturer's protocol. Upon completion of staining, cells were stored in fresh 1% methanol-free formaldehyde in PBS (Thermo Fisher Scientific) until the day of data collection. Just before data collection, all cells were labeled with rhodium (Fluidigm) at 1:1000 for 45 minutes at room temperature. All events were acquired on a Helios mass cytometer (Fluidigm). Mass cytometry data were acquired at the University of Maryland School of Medicine Center for Innovative Biomedical Resources Flow Cytometry and Mass Cytometry Core Facility, Baltimore, Maryland.

Mass cytometry data preprocessing. Randomization, bead normalization, and bead removal of data collected were performed on CyTOF software (Fluidigm) v6.7. Using FlowJo (BD) v10.5, single-cell events were

identified by gating a tight population based on cell length and rhodium signal. Dead cells were then eliminated by manually gating out cells positive for 106Pd and 108Pd on a biaxial plot. Debarcoding was carried out by manual gating to select for events that were singly positive for the barcode of interest and doubly negative for the remaining 2. Each individual preprocessed sample was exported as a separate fcs file for analysis.

Flow cytometry. For control comparisons between tumor-bearing mice without isotype treatments and tumor-bearing mice with isotype treatments, fluorescent flow cytometry with the following panel was used: anti-CD3 Pacific Blue (145-2C11, BioLegend, 1:50), anti-CD4 BV605 (RM4-5, BD, 1:200), anti-CD8 BV786 (53-6.7, BD, 1:200), anti-CD19 APC (6D5, BioLegend, 1:200), anti-CD23 Alexa Fluor 700 (B3B4, BioLegend, 1:100), and anti-CD21 APC/Cy7 (7E9, BioLegend, 1:200). Briefly, single-cell suspensions from lymph nodes were Fc blocked for 10 minutes at 4°C, after which the samples were incubated in the antibody cocktail in FACS buffer for 30 minutes at 4°C. Cells were washed twice with FACS buffer, and data were collected on CytoFLEX (Beckman Coulter). All supervised gating analyses were performed on Cytobank.

Identification and visualization of clusters from mass cytometry data sets. Both unsupervised and hierarchal gating analyses were performed in parallel. For unsupervised analysis, a modified analysis pipeline from Nowicka et al. (37) was utilized using R v3.5. FlowSOM algorithm (38) was used to define 20 metaclusters for T cell subtyping analysis and 25 metaclusters for B cell subtyping analysis. Resulting metaclusters from the respective data sets were annotated into 7 final T cell subtypes and 10 final B cell subtypes. These clusters were then visualized using a 2-dimensional UMAP dimensional reduction algorithm (39) separately for T cell and B cell subtype data sets. Two thousand cells per sample were used for visualization. Cluster proportions from each lymph node were also converted into absolute cell numbers of each cell type by multiplying the quantified total number of cells from the corresponding lymph node. Tables in csv format for cluster proportions were outputted for statistical analyses (Supplemental Tables 3 and 4). Expression levels of functional markers, CD69, CD40, CTLA4, PD-1, PD-L1, BTLA, IFN-γ, TNF-α, and IL-2, were compared as median intensities across clusters and groups (Supplemental Tables 5 and 6). For hierarchal gating analysis, preprocessed fcs files were imported into Cytobank. All gating hierarchies for T cell subtypes and B cell subtypes are shown in Supplemental Figures 2 and 3, respectively. Functional markers were analyzed by gating for positive populations based on biaxial plot visualizations for every T cell subtype and B cell subtype.

Statistics. To compare the means of the 3 groups, as proportions, numbers, or median expression values, while taking into account any potential differences related to the multiplex batching, we performed repeated-measures 1-way ANOVA followed by pairwise testing between the groups. Adjusted *P* values (FDR) of less than 0.05 were considered statistically significant.

Study approval. Experiments were performed in accordance with protocols approved by the institutional Animal Care and Use Committee of Johns Hopkins University.

Author contributions

WJH performed the experiments, developed experimental and analytical methods, analyzed data, and wrote the manuscript. MY assisted with data analysis and edited the manuscript. SC performed the experiments, assisted with data analysis, and reviewed the manuscript. RMM assisted with developing analytical methods and reviewed the manuscript. MBS assisted with experimental methods and reviewed the manuscript. LD developed analytical methods and reviewed the manuscript. EJF supervised analytical method development and reviewed the manuscript. EMJ supervised the design and analysis of all experiments and reviewed and edited the manuscript.

Acknowledgments

WJH is the recipient of the American Society of Clinical Oncology Young Investigator Award and American Association of Cancer Research Incyte Immuno-Oncology Research Fellowship and is supported by NIH T32CA00971-38. The research is also supported by Hopkins-Allegheny Health Network Cancer Research Fund. The authors also thank Felix J. Hartmann and the Bendall lab for technical advice.

Address correspondence to: Elizabeth E. Jaffee, 1830 East Monument Street, Room 4M07 Cancer Research Building I, Suite 2-103, Baltimore, Maryland 21205, USA. Phone: 410.955.2957; Email: ejaffee@jhmi.edu.

1. Ghiringhelli F, et al. Tumor cells convert immature myeloid dendritic cells into TGF-beta-secreting cells inducing CD4+CD25+ regulatory T cell proliferation. *J Exp Med*. 2005;202(7):919–929.
2. Huang SC, et al. TGF-β1 secreted by Tregs in lymph nodes promotes breast cancer malignancy via up-regulation of IL-17RB. *EMBO Mol Med*. 2017;9(12):1660–1680.
3. Alonso R, et al. Induction of anergic or regulatory tumor-specific $CD4^+$ T cells in the tumor-draining lymph node. *Nat Commun*. 2018;9(1):2113.
4. Hiura T, et al. Both regulatory T cells and antitumor effector T cells are primed in the same draining lymph nodes during tumor progression. *J Immunol*. 2005;175(8):5058–5066.
5. Harrell MI, Iritani BM, Ruddell A. Tumor-induced sentinel lymph node lymphangiogenesis and increased lymph flow precede melanoma metastasis. *Am J Pathol*. 2007;170(2):774–786.
6. Habenicht LM, Albershardt TC, Iritani BM, Ruddell A. Distinct mechanisms of B and T lymphocyte accumulation generate tumor-draining lymph node hypertrophy. *Oncoimmunology*. 2016;5(8):e1204505.
7. Jeanbart L, et al. Enhancing efficacy of anticancer vaccines by targeted delivery to tumor-draining lymph nodes. *Cancer Immunol Res*. 2014;2(5):436–447.
8. Rohner NA, et al. Lymph node biophysical remodeling is associated with melanoma lymphatic drainage. *FASEB J*. 2015;29(11):4512–4522.
9. Ganti SN, Albershardt TC, Iritani BM, Ruddell A. Regulatory B cells preferentially accumulate in tumor-draining lymph nodes and promote tumor growth. *Sci Rep*. 2015;5:12255.
10. Schwartz M, Zhang Y, Rosenblatt JD. B cell regulation of the anti-tumor response and role in carcinogenesis. *J Immunother Cancer*. 2016;4:40.
11. Shu S, Cochran AJ, Huang RR, Morton DL, Maecker HT. Immune responses in the draining lymph nodes against cancer: implications for immunotherapy. *Cancer Metastasis Rev*. 2006;25(2):233–242.
12. Thomas SN, Vokali E, Lund AW, Hubbell JA, Swartz MA. Targeting the tumor-draining lymph node with adjuvanted nanoparticles reshapes the anti-tumor immune response. *Biomaterials*. 2014;35(2):814–824.
13. Topalian SL, et al. Safety, activity, and immune correlates of anti-PD-1 antibody in cancer. *N Engl J Med*. 2012;366(26):2443–2454.
14. Pardoll DM. The blockade of immune checkpoints in cancer immunotherapy. *Nat Rev Cancer*. 2012;12(4):252–264.
15. Fransen MF, et al. Tumor-draining lymph nodes are pivotal in PD-1/PD-L1 checkpoint therapy. *JCI Insight*. 2018;3(23):124507.
16. Juneja VR, et al. PD-L1 on tumor cells is sufficient for immune evasion in immunogenic tumors and inhibits CD8 T cell cytotoxicity. *J Exp Med*. 2017;214(4):895–904.
17. Bendall SC, et al. Single-cell mass cytometry of differential immune and drug responses across a human hematopoietic continuum. *Science*. 2011;332(6030):687–696.
18. Mosely SI, et al. Rational selection of syngeneic preclinical tumor models for immunotherapeutic drug discovery. *Cancer Immunol Res*. 2017;5(1):29–41.
19. Mauri C, Menon M. The expanding family of regulatory B cells. *Int Immunol*. 2015;27(10):479–486.
20. Bruno TC, et al. Antigen-presenting intratumoral B cells affect $CD4^+$ TIL phenotypes in non-small cell lung cancer patients. *Cancer Immunol Res*. 2017;5(10):898–907.
21. Yuen GJ, Demissie E, Pillai S. B lymphocytes and cancer: a love-hate relationship. *Trends Cancer*. 2016;2(12):747–757.
22. Calzascia T, et al. TNF-alpha is critical for antitumor but not antiviral T cell immunity in mice. *J Clin Invest*. 2007;117(12):3833–3845.
23. Trevejo JM, et al. TNF-alpha -dependent maturation of local dendritic cells is critical for activating the adaptive immune response to virus infection. *Proc Natl Acad Sci USA*. 2001;98(21):12162–12167.
24. Ye LL, Wei XS, Zhang M, Niu YR, Zhou Q. The significance of tumor necrosis factor receptor type II in $CD8^+$ regulatory T cells and $CD8^+$ effector T cells. *Front Immunol*. 2018;9:583.
25. Kearney CJ, et al. Tumor immune evasion arises through loss of TNF sensitivity. *Sci Immunol*. 2018;3(23):eaar3451.
26. Yang S, et al. Differential roles of TNFα-TNFR1 and TNFα-TNFR2 in the differentiation and function of $CD4^+Foxp3^+$ induced Treg cells in vitro and in vivo periphery in autoimmune diseases. *Cell Death Dis*. 2019;10(1):27.
27. Urbano PCM, Koenen HJPM, Joosten I, He X. An autocrine TNFα-tumor necrosis factor receptor 2 loop promotes epigenetic effects inducing human treg stability *in vitro*. *Front Immunol*. 2018;9:573.
28. Zhao X, et al. TNF signaling drives myeloid-derived suppressor cell accumulation. *J Clin Invest*. 2012;122(11):4094–4104.
29. Bertrand F, et al. TNFα blockade overcomes resistance to anti-PD-1 in experimental melanoma. *Nat Commun*. 2017;8(1):2256.
30. Perez-Ruiz E, et al. Prophylactic TNF blockade uncouples efficacy and toxicity in dual CTLA-4 and PD-1 immunotherapy. *Nature*. 2019;569(7756):428–432.
31. Chung Y, et al. CD1d-restricted T cells license B cells to generate long-lasting cytotoxic antitumor immunity in vivo. *Cancer Res*. 2006;66(13):6843–6850.
32. Bae EA, et al. Activation of NKT cells in an anti-PD-1-resistant tumor model enhances antitumor immunity by reinvigorating exhausted CD8 T cells. *Cancer Res*. 2018;78(18):5315–5326.
33. Cervera-Carrascon V, et al. TNFa and IL-2 armed adenoviruses enable complete responses by anti-PD-1 checkpoint blockade. *Oncoimmunology*. 2018;7(5):e1412902.
34. Han G, Spitzer MH, Bendall SC, Fantl WJ, Nolan GP. Metal-isotope-tagged monoclonal antibodies for high-dimensional mass cytometry. *Nat Protoc*. 2018;13(10):2121–2148.
35. Lin D, Gupta S, Maecker HT. Intracellular cytokine staining on PBMCs Using CyTOF™ mass cytometry. *Bio Protoc*. 2015;5(1):e1370.
36. Hartmann FJ, Simonds EF, Bendall SC. A universal live cell barcoding-platform for multiplexed human single cell analysis. *Sci Rep*. 2018;8(1):10770.
37. Nowicka M, et al. CyTOF workflow: differential discovery in high-throughput high-dimensional cytometry data sets. *F1000Res*. 2017;6:748.
38. Van Gassen S, et al. FlowSOM: Using self-organizing maps for visualization and interpretation of cytometry data. *Cytometry A*. 2015;87(7):636–645.
39. Becht E, et al. Dimensionality reduction for visualizing single-cell data using UMAP. *Nat Biotechnol*. 2019;37:38–44.